Supplementary Materials

Short-range and long-range order of phyllomanganate nanoparticles determined using high energy X-ray scattering

Alain Manceau, Matthew A. Marcus, S. Grangeon, M. Lanson, B. Lanson, A-C. Gaillot, S. Skanthakumar and L. Soderholm

Note S1. Bragg-rod calculation details

In this section, we report selected details of the Bragg-rod calculation that did not appear in the main text, including the consideration of further simulation features not used in the current study but which could be used later to take advantage of the full power of CALCIPOW (Plançon, 2002), if desired. In order to make its use easier, an interactive program ("wrapper") was written in LabVIEW (National Instruments, Austin TX, USA) which generates the input files, calls CALCIPOW, and reads the resulting output. The details to be filled out for each atom in the input file are its occupancy, atomic number, position, and a table of the scattering factor versus $\sin\theta / \lambda$. In addition, there is a section which describes layer stacking because CALCIPOW can handle everything from fully turbostratic layers to fully three-dimensional crystals, with intermediate cases described in terms of random and defined stacking faults (Lanson et al., 2002a). In our case, we only needed the fully-turbostratic description, but the wrapper includes the possibility of the aforementioned types of layer ordering. Similarly, the program can handle the specific case of preferred orientation normal to the scattering vector, so it requires the orientation distribution function as a function of angle from the normal. The program also needs the CSD size and the log-normal distribution parameters for the number of layers per particle, in order to predict the 00*l* reflections. All of these clerical functions are handled by the wrapper.

In addition, the program requires a table of the T(U) function of Drits and Tchoubar (1990). This function is a scaled Fourier transform of the overlap function of the particle in the transverse dimension. This overlap function represents the fraction of the layer area that is overlapped by a copy of the layer shifted by a given distance. In the case of anisometric particles, T(U) is the orientation average of the Fourier transform of the overlap function with the shift taken in differing directions. To simulate the effect of a distribution of particle size, we considered that the shape of the Bragg rod for a layer of any transverse size is constant, with only the scale factor in q changing. Thus, if the particle is big enough transversely, so that the radius of the Bragg rod is small compared with that of the Ewald sphere, doubling the CSD size in the layer plane will halve the width of the peak in *I(q)* without changing its shape. This effect may be simulated in CALCIPOW

by replacing T(U) with T(2U), for instance. Thus, if one has a distribution of particle sizes, then T(U) may be replaced by an integral over the distribution $\int d\lambda\, p(\lambda)\mathrm{T}(\mathrm{U}\lambda)$ where $p(\lambda)$ is the probability density function for particles of size λCSD_0, with CSD_0 being the nominal size specified for CALCIPOW. With a log-normal distribution for $p(\lambda)$, we used Gauss-Hermite quadrature to perform the integration and get the effective T(U). If the CSD is circular, that is all we have to do because T(U) for a circle is known analytically. However, for other shapes, one needs to perform other operations to get T(U), which will be summarized only briefly because only circular domains were used in the present investigation. For a general polygonal domain, we can raster the polygon and perform the integral as a sum over line segments, then use Equation 2.20 of Drits and Tchoubar (1990) to calculate the contribution from each line segment. The lengths of these line segments will depend on the direction over which one integrates, hence on the orientation of the scattering vector with respect to the domain. Since we want a powder average, we simply average the T(U) function over a number of angles, typically three.

CALCIPOW allows sites to have fractional occupation, which makes it easy to treat vacancies in an approximate way. However, as mentioned in the main text, if one tries to use the chalcophanite model with ordered vacancies, one winds up with superlattice reflections that are as sharp as the other reflections, whereas the DE model yields only broad bumps due to the short-range nature of the vacancy ordering. Thus, we used the simple unit cell for which parameters are given in Tables 4 and 5.

In order to model strain, we used a *q*-dependent CSD size. The list of reflections is sorted by |*q*|, and a set of CALCIPOW input files is made, one for each value of |*q*|. These files differ only in the list of reflections to be calculated and the CSD. CALCIPOW is then run for each of these files and the resulting intensities added together.

It is probably too complex to implement a stable efficient algorithm for the Bragg-rod fitting that includes all crystallographic, non-uniform, and anisotropic parameters in turbostratic nanocrystals. Therefore, parameter values were optimized by exploring parameter space manually by trial-and-error by varying systematically a set of parameter values. Structural constraints were enforced by varying progressively as a function of pH the amounts of vacancies and interlayer species for the three δ-MnO_2 samples, so as to describe these nanomaterials using a unifying framework with only a minimum number of parameters.

Note S2. Debye Equation calculation details

S.2.1. Structural specification

The initial structure is based on a triangular lattice of MnO_6 octahedra (the layer), which is truncated to the boundary of the CSD, in our case a circle of a given size. Then, modifications are introduced as follows:

1. Layer vacancies. A given fraction of Mn atoms are left out at random. However, it is assumed for crystal chemical reasons that no two vacancies may be nearest neighbors. Therefore, sets of vacancies are tossed until a structure meeting this condition is found.
2. Vacant sites may be capped with Mn_{IL} atoms. It is forbidden for a vacancy to be capped both above and below, because short-distance Mn_{IL}-Mn_{IL} pairs are excluded from an inspection of the PDF correlations. Each Mn_{IL} atom is provided with three water molecules in the interlayer (represented by oxygens) in addition to the three layer oxygens (O_L) to which it is attached.
3. Interlayer and mid-layer Na and water molecules are added at random sites, making sure that they do not get too close to each other. Minimum distances allowed for atom pairs are Na-(O, water), 2Å, Mn-(O, water), 1.5Å, Na-Mn, 2Å.
4. If it is desired to keep Mn_{IL} from coming too close to each other (see below), then structures are generated according to the above steps until no such unwanted pairs occur.
5. The layer is "bent" to simulate the bending seen in TEM studies. The layer is bent around a spherical or cylindrical mandrel such that the neutral plane is the layer plane $z = 0$. This bending is parameterized by the reciprocal bending radii in x and y directions (supplementary information, note S2).

Because vacancies and all other atoms, except for Mn_L and O_L, occur at random sites, the diffraction from each instance of the structure with given specifications has significant fluctuations. Therefore, we averaged over 100-1000 such structures. This averaging also gives us the opportunity to add polydispersity of layer (CSD) size by generating structures of different sizes for which the intensities are averaged. The positional and "thermal" parameters of the atoms were taken from the Bragg-rod fits.

We did not attempt to model multilayered particles because such modeling would require the explicit generation of atomic positions and interatomic distances for all layers, which would have increased the calculation time and memory requirements by a large factor for a relatively small gain in understanding (the 00*l* reflections).

S.2.2. Calculation

As Cervellino *et al.* (2010) and others have found, it is impractical to compute the sinc function for each pair of atoms in the double sum over atom pairs and all q-values. Instead, we assembled the distances into a set of histograms, one for each pair of atom types. Here, because atoms of a given element such as Mn, but in different sites (Mn_L, Mn_{IL}), may have different Debye-Waller factors, we counted such atoms as different and assigned them their own histograms. Thus, there is a histogram for Mn_L-O distances, and one for Mn_{IL}-O distances. We took the bin size to be 0.01-0.02 Å. In partial compensation for the discreteness of the histogram bins, we assigned each distance partial membership in the two bins adjacent to it. For example, if there were histogram bins centered at 2.80 Å and 2.81 Å and there was a pair of atoms 2.804 Å apart, we assigned this pair 0.6 membership in the 2.80 Å bin and 0.4 in the 2.81 Å bin. Compared with doing the

exact summation, this procedure is like applying a broadening function with a width that varies depending on how close a distance is to a bin center, but is never more than the bin width. The mean distance in the histogram thus preserves the mean distance in the exact distribution.

We took advantage of the regular tabulation of distances and *q*-values by using trigonometric recursion relations to compute all values of $\sin(qr)/qr$ once, with minimal evaluation of trig functions. Thus, when computing the diffraction from multiple structures, we only needed calculate these factors once. We then used these factors to compute all values of $f_i f_j \ \mathrm{sinc}(qr)$. The scattering factors f_i for neutral atoms and water molecules (approximated as oxygens) were computed from the Waasmaier and Kirfel (1995) forms as mentioned for the Bragg-rod method. No anomalous dispersion corrections to the coherent atomic scattering factors were introduced.

The description given in the main text is for a model we refer to as "correlated" occupancy, in which each site is either occupied or empty for a given realization of the model, and in which rules about vacancies not neighboring other vacancies and atoms not coming too close to other atoms are obeyed. Another version of the model is what we refer to as "binary" occupancy, in which sites are populated at random, with no regard to crystal-chemical rules. This type of model comes closer to what the Bragg-rod model simulates than does "correlated" occupancy. We also considered "fractional" occupancy, in which we simulate a given probability for each occupied site, with said probability uncorrelated with the occupation of any other site, and perform an analytical average over these occupancies. This can be considered a DE version of the way fractional occupancy is treated in the Bragg-rod case. In this case, we can extend the DE (4) by assuming that each atom *i* is present with probability p_i, or absent, and that its presence or absence does not affect the position or occupancy of any other site. In that case, we consider the scattering factor f_i to be a random variable which has either its usual value, with probability p_i or vanishes with probability $1-p_i$, so that the Debye equation is modified to:

$$I = \frac{1}{N_L}\left[\sum_{i=1}^{N_L} p_i \,|\, f_i \,|^2 + 2\sum_{i=2}^{N_L}\sum_{j=1}^{i-1} p_{ij}\,\mathrm{Re}(f_i f_j^*)\,\frac{\sin(q\,|\,\vec{r}_i-\vec{r}_j\,|)}{q\,|\,\vec{r}_i-\vec{r}_j\,|}\exp\left(-(U_i+U_j)q^2/2\right)\right] \qquad \text{(S1)}$$

where p_{ij} is the probability that both atoms *i* and *j* are present. If we assume uncorrelated occupancy, then $p_{ij} = p_i p_j$. Note that $p_{ii} = p_i$, hence the lack of an exponent on p_i in the first term. A comparison of these three modes of modeling for dBi10 and dBi3 is shown in Figure S1. The "binary" and "fractional" models yield near-identical results for the two pH samples, the "correlated " model gives slightly different results at pH 10, and even more so at pH 3 owing to the abundance of Mn_{IL}.

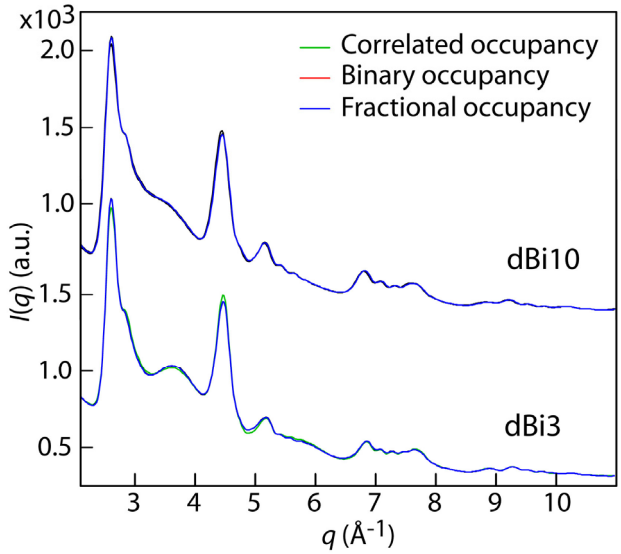

Figure S1. *hk* XRD bands calculated with the strained-layer values given in Table 5 for three possible occupancy models: correlated, binary, and fractional.

S.2.3. Strain

The bending of the layer over a spherical "mandrel" was handled as follows: Let the original Cartesian coordinates of an atom be $x_0.y_0, z_0$ with the *z*-axis normal to the layer, and let R_0 be the bend radius. Then, we performed the following set of operations to "wrap" the structure around the sphere of radius R_0 :

$$\begin{aligned}
&\rho = \sqrt{x_0^2 + y_0^2} \\
&\theta = \rho / R_0 \\
&R = R_0 + z_0 \\
&x_{bent} = R(x/\rho)\sin\theta \quad y_{bent} = R(y/\rho)\sin\theta \\
&z_{bent} = z_0\cos\theta - R_0\sin^2\theta/(1+\cos\theta) \quad .
\end{aligned} \tag{S2}$$

The first two lines express the transverse position in polar coordinates. Then, x_{bent}, y_{bent} are computed as the transverse position of the end of an arc that subtends an angle θ as seen from the center of curvature and extending in the azimuthal direction of x_0, y_0 . The last line gives the position "above" or "below" the sphere, in a form which does not run into numerical problems at large R_0 . Similar formulas can be implemented for cylindrical and ellipsoidal bends.

For a cylindrical bend around the *x*-axis, the corresponding equations are

$$\begin{aligned}
&\phi = x_0 / R_0 \\
&R = R_0 + z_0 \\
&x_{bent} = R\sin\phi \\
&y_{bent} = y_0 \\
&z_{bent} = z_0\cos\phi - 2R_0\sin^2(\phi/2)
\end{aligned} \tag{S3}$$

It should be noted that these forms do not take into account anything about the mechanical properties of the layer. In particular, anticlastic bending is not included in the above cylindrical-bend formulas, and neither bend prescription accounts for Poisson-like coupling of in-plane and out-of-plane strain.

S.2.4. Fitting

In principle, if the experimental measurements were performed on monodisperse single-layer particles, and the background subtracted, then the calculated diffraction intensity should match experiment up to a constant factor. In practice, the contributions from the multi-layered nature of the particles, plus inter-particle interference, means that there will always be a background, assumed to be slowly-varying in q, which the calculation cannot match. Thus, we fit the data using the polynomial form described for the Bragg-rod method (2).

Best fits were found by searching parameter space. We started with the values derived by hand-optimizing the match in the Bragg-rod calculation, after which we did more manual searching, one or two parameters at a time. The obvious thing to try in order to get a better fit than from manual searching is to use a non-derivative minimizer to search parameter space. However, the function being minimized is noisy because of the structure randomness. Thus, we used a brute-force approach in which we defined parameter ranges and simply tossed up to 1000 sets of parameter values within these ranges. This method produced what seems to be a slightly better fit than was obtained in the initial manual searches. By doing such a search over just two parameters at a time (e.g. b and strain), we could fit the normalized sum-squared error (*NSS*) to a quadratic function of these parameters, thus pinpointing the true minimum and getting an idea of parameter correlations. Because the fractional-occupancy model involves a unique structure for each parameter set, it is faster to compute than either the binary- or correlated-occupancy models and does not introduce statistical noise into the evaluation of the goodness of fit. Therefore, we found it useful to perform the parameter search in the fractional-occupancy model, then redo it in a smaller region of parameter space for the other types of occupancy.

Table S1

Atom parameters from the PDF analysis.

U values for dBi3, dBi6 and dBi10 were averaged, and crystallographic coordinates kept identical at all pHs. O_{IL} are structural water molecules coordinated to Mn_{IL}. Their occupancies are three times the Mn_{IL} occupancy. The Mn_L and Mn_{IL} cation occupancies were linked according to layer-interlayer charge balance, and the Na/K occupancy fixed from chemical analysis (values given in Table 1 for dBi).

	x	y	z	$U_{11,22}$ (Å^2)	U_{33} (Å^2)	Occ.
KBi8 – XRD						
Mn_L	0	0	0			0.88

O_L	2/3	1/3	0.070			2.0
Mn_{IL}	0	0	0.150			0.08
O_{IL}	1/3	2/3	1/4			0.24
K	0.24	0.76	1/4			0.23
H_2O	0.225	0.113	1/4			0.36
KBi8 – PDF model 1						
Mn_L	0†	0†	0†	0.003‡[1]	0.012	0.92
O_L	2/3†	1/3†	0.068	0.006	0.029	2.0†
Mn_{IL}	0†	0†	0.150	0.003‡[1]	0.003‡[1]	0.03
O_{IL}	1/3†	2/3†	1/4	0.060‡[2]	0.060‡[2]	0.09
K	0.292§	0.708§	1/4	0.060‡[2]	0.060‡[2]	0.23†
H_2O	0.274§	0.137§	1/4	0.060‡[2]	0.060‡[2]	0.36†
KBi8 – PDF model 2						
Mn_L	0†	0†	0†	0.003‡[1]	0.012	0.92
O_L	2/3†	1/3†	0.068	0.006	0.029	2.0†
Mn_{IL}	0†	0†	0.154	0.003‡[1]	0.003‡[1]	0.03
O_{IL}	1/3†	2/3†	1/4	0.050‡[2]	0.050‡[2]	0.09
K	0.24†	0.76†	1/4	0.050‡[2]	0.050‡[2]	0.23†
H_2O	0.225†	0.113†	1/4	0.050‡[2]	0.050‡[2]	0.36†
NaBi – XRD						
Mn_L	0	0	0			1.0
O_L	0.389	0.627	0.140			2.0
Na_{IL}	0.628	0.476	0.481			0.31
H_2O	0.291	0.180	0.496			0.40
NaBi – Model 1						
Mn_L	0†	0†	0†	0.002	0.016	1.0†
O_L	0.376	0.605	0.134	0.005	0.167	2.0†
Na_{IL}	0.697	0.568	0.510	0.023‡	0.023‡	0.31†
H_2O	0.158	0.199	0.516	0.023‡	0.023‡	0.40†
NaBi – Model 2						
Mn_L	0†	0†	0†	0.002	0.016	1.0†
O_L	0.390	0.626	0.130	0.007	0.104	2.0†
Na_{IL}	0.628†	0.476†	0.481†	0.013‡	0.013‡	0.31†
H_2O	0.291†	0.180†	0.496†	0.013‡	0.013‡	0.40†
dBi						
Mn_L	0.715	0.576	-0.008	0.0012‡[1]	0.0021‡[2]	
O_L	0.525	0.623	0.139	0.0014	0.033	1.0†
O_L	0.250	0.196	0.135	0.0014	0.033	1.0†
O_L	2/3†	1/3†	0.125	0.0014	0.033	1.0†
Mn_{IL}	-0.007	0.017	0.290	0.0012‡[1]	0.0021‡[2]	
O_{IL}	0.179	0.931	0.443	0.0018‡[3]	0.0018‡[3]	
Na	0.950†	0.650†	0.5	0.0018‡[3]	0.0018‡[3]	
Na	0.324	0.963	0.5	0.0018‡[3]	0.0018‡[3]	
H_2O	0.575†	0.260†	0.5	0.0018‡[3]	0.0018‡[3]	1.0†
H_2O	0.425†	0.545†	0.5	0.0018‡[3]	0.0018‡[3]	1.0†

† Fixed. ‡ Kept equal. § Covaried from space group symmetry.

Table S2

Parameters from three equivalent best-fits of the AcidBir PDF in space group *C*12/*m1*.

c was fixed to 7.32 Å, q_{damp} to 0.045 Å^{-1}, q_{broad} to 0.069 Å^{-1}, Mn_L Occ. to 0.94, K Occ. to 0.26, and H_2O Occ. to 0.77 as in Zhu *et al.* (2012). K and H_2O were allowed to deviate from their mid-layer position to increase the flexibility of the model-fit.

		Parameters from Zhu *et al.* (2012)	Model 1 ($a \neq b\sqrt{3}$) ‡	Model 2 ($a = b\sqrt{3}$) ‡	Model 3 ($a = b\sqrt{3}$) §
a (Å)		4.942	4.919	4.923	4.922
b (Å)		2.829	2.845	-	-
a/*b*		1.747	1.729	1.732†	1.732†
β (°)		96.02	96.24	96.13	95.75
Scale		1.27	1.36	1.37	1.27
δ_2		3.45	3.28	3.27	3.37
Diameter (Å)		-	78.7	71.8	94.8
Mn_L	U_{11}	0.011	0.002	0.003	0.001
x=0, *y*=0, *z*=0	U_{22}	0.0029	0.003	0.003	0.005
	U_{33}	0.27	0.163	0.167	0.194
O_L	*x*	0.349	0.349	0.349	0.347
y=0	*z*	0.131	0.135	0.134	0.134
	U_{11}	0.005	0.005	0.003	0.004
	U_{22}	0.007	0.008	0.009	0.004
	U_{33}	0.11	0.037	0.035	0.033
K	*x*	0.112	0.141	0.103	0.840
y=0	*z*	0.556	0.506	0.565	0.594
	U_{iso}	0.009	0.079	0.037	0.012
H_2O	*x*	0.521	0.450	0.497	0.209
y=0	*z*	0.553	0.533	0.547	0.529
	U_{iso}	0.019	0.218	0.010	0.003
R_w (%)		20.8	21.0	21.2	20.8

‡ K, H_2O positions close to Zhu *et al.* (2012). § K, H_2O positions close to KBi8. † Fixed.